Triaxial rotor modes in finite-N boson systems

Yu Zhang,[1] Sheng-Nan Wang,[1] Feng Pan,[1,2] Chong Qi,[3] and J. P. Draayer[2]
[1]*Department of Physics, Liaoning Normal University, Dalian 116029, People's Republic of China*
[2]*Department of Physics and Astronomy, Louisiana State University, Baton Rouge, Louisiana 70803-4001, USA*
[3]*Department of Physics, KTH Royal Institute of Technology, Stockholm 10691, Sweden*

(Received 13 May 2024; accepted 26 July 2024; published 8 August 2024)

We propose an algebraic approach to elucidate the dynamic characteristics of triaxial rotor modes in nuclei by mapping a triaxial rotor Hamiltonian to the interacting boson model one within a finite-N framework. Our method unveils striking features not observed in conventional modes, exemplified by the $B(E2)$ anomaly, characterized by $B(E2;4_1^+ \to 2_1^+)/B(E2;2_1^+ \to 0_1^+) < 1$. Using specific examples, we demonstrate that the peculiar properties of low-lying states in both neutron-rich and neutron-deficient Os nuclei can be comprehensively understood through the proposed Hamiltonian, which incorporates both rigid and soft triaxial rotor modes. This algebraic method not only offers fresh insights into triaxial dynamics but also showcases its capability in uncovering emergent exotic collective modes in nuclear structure.

DOI: 10.1103/PhysRevC.110.024303

I. INTRODUCTION

The emergence of collective modes stands as a pivotal characteristic of complex nuclear many-body systems. The systems with quadrupole deformation, in particular, exhibit several typical collective modes, such as the spherical vibrator, γ-unstable rotor, and deformed rotors (whether axial or triaxial). These collective modes represent the quantum mechanical expression of distinct intrinsic deformations inherent to nuclear systems [1]. The investigation of rotor modes in finite-N systems has been a compelling pursuit since Elliott's groundbreaking work, which provided a microscopic elucidation of rotational spectra in light nuclei [2]. Based on the algebraic relations [3], it was demonstrated that triaxial rotor dynamics can be microscopically elucidated through the SU(3) framework of the shell model [4,5]. Similarly, the algebraic realization of rotor modes has been attained within the SU(3) limit of the interacting boson model (IBM) [6]. An exact mapping scheme for the IBM realization [7] has been recently applied to explicate anomalous $E2$ transitions observed in neutron-deficient triaxial nuclei [8]. These endeavors underscore the intimate connection between rotor modes and SU(3) symmetry within nuclei [9].

The IBM [10] exhibits remarkable efficacy in elucidating collective modes within nuclei. Its notable advantage lies in its ability not only to encompass a few distinct and fundamental collective limits but, more crucially, to employ a simple Hamiltonian formulation [11] for investigating broader scenarios involving the mixing or transitions among various collective modes. However, the description of triaxial rotor modes, often employed in interpreting nuclear collective excitations [12], presents a challenge within the IBM due in part to the inability of the model to straightforwardly account for triaxial deformations via two-body terms. To address this limitation, one approach involves incorporating higher-order interactions [13]. For instance, the inclusion of a cubic term $(d^\dagger \times d^\dagger \times d^\dagger)^3 \cdot (\tilde{d} \times \tilde{d} \times \tilde{d})^3$ [13,14] yields a potential surface with a stable triaxial minimum at $\gamma = 30^\circ$, enhancing the IBM's description of triaxial nuclei [15,16]. Additionally, it has been shown [17] that a parameter region of triaxiality within $0^\circ < \gamma < 60^\circ$ can be accommodated in the extended consistent-Q formalism, incorporating a cubic term in the quadrupole operators. Broadly speaking, a scalar polynomial in the quadrupole operators can be used to generate triaxial deformation within the IBM at the mean-field level [8,18]. Notably, the rotor image within the IBM [6,7] can be straightforwardly constructed using symmetry-conserving operators from the SU(3) $\supset$ SO(3) integrity basis, employing a scalar polynomial in the quadrupole operators [7,8]. Despite achieving an algebraic realization within the SU(3) limit of the IBM, the impact of rotor modes on IBM dynamics remains to be fully elucidated. Particularly, a model analysis addressing the interplay between triaxial rotor and other collective modes is warranted, given that realistic nuclear systems often entail multiple collective modes.

In this work, we undertake a comprehensive examination of the IBM formulation of the triaxial rotor mode and its corresponding dynamics. Through this investigation, we aim to shed light on the pivotal role of the triaxial rotor in the IBM depiction of triaxial nuclei, particularly concerning anomalous $E2$ phenomena. Additionally, we endeavor to identify a unified framework capable of encompassing all typical collective modes, including the triaxial rotor, thus offering a cohesive description of nuclear dynamics.

II. COLLECTIVE MODES IN THE IBM

The IBM Hamiltonian is constructed from two kinds of boson operators, namely, the s boson with $l^\pi = 0^+$ and the d boson with $l^\pi = 2^+$ [10]. The total boson number N is

taken as the number of valence particle or hole pairs for a given nucleus. Three dynamical symmetry limits in the IBM are characterized by three different group chains of the U(6) group [10]:

$$\mathrm{U}(6) \supset \mathrm{U}(5) \supset \mathrm{O}(5) \supset \mathrm{O}(3), \tag{1}$$

$$\mathrm{U}(6) \supset \mathrm{SU}(3) \supset \mathrm{O}(3), \tag{2}$$

$$\mathrm{U}(6) \supset \mathrm{O}(6) \supset \mathrm{O}(5) \supset \mathrm{O}(3). \tag{3}$$

Dynamical symmetry associated with each group chain corresponds to a typical nuclear shape or collective mode, including the spherical vibration in the U(5) limit, the axially symmetric rotation in the SU(3) limit, and the γ-unstable motion [19] in the O(6) limit. To describe these modes, it is convenient to adopt the consistent-Q Hamiltonian, which is written as [11]

$$\hat{H}_{\mathrm{CQ}} = \varepsilon\, \hat{n}_d + \tfrac{\kappa}{N} \hat{Q}^{\chi} \cdot \hat{Q}^{\chi} \tag{4}$$

with

$$\hat{n}_d = d^{\dagger} \cdot \tilde{d}, \tag{5}$$

$$\hat{Q}^{\chi}_u = (d^{\dagger} s + s^{\dagger} \tilde{d})^{(2)}_u + \chi (d^{\dagger} \times \tilde{d})^{(2)}_u, \tag{6}$$

where ε, κ, χ are real parameters, and N is the total number of the bosons. The three dynamical symmetry limits of the consistent-Q Hamiltonian (4) can be characterized as: the U(5) limit for $\varepsilon > 0$ and $\kappa = 0$; the O(6) limit for $\varepsilon = 0$, $\kappa < 0$, and $\chi = 0$; and the SU(3) limit for $\varepsilon = 0$, $\kappa < 0$, and $\chi = \pm\sqrt{7}/2$. To elucidate the geometric aspects of the IBM, one can examine its classical limit by employing the coherent state defined by [10]

$$|\beta, \gamma, N\rangle = N_A \left[s^{\dagger} + \beta \cos\gamma\, d^{\dagger}_0 + \frac{1}{\sqrt{2}} \beta \sin\gamma (d^{\dagger}_2 + d^{\dagger}_{-2}) \right]^N |0\rangle \tag{7}$$

with $N_A = 1/\sqrt{N!(1+\beta^2)^N}$. The classical potential corresponding to $\hat{H}_{\mathrm{CQ}}$ is thus given by

$$\begin{aligned} V_{\mathrm{CQ}}(\beta, \gamma) &= \frac{1}{N} \langle \beta, \gamma, N | \hat{H}_{\mathrm{CQ}} | \beta, \gamma, N \rangle |_{N \to \infty} \\ &= \varepsilon \frac{\beta^2}{1+\beta^2} + \kappa \frac{1}{(1+\beta^2)^2} \\ &\quad \times \left[4\beta^2 - 4\sqrt{\frac{2}{7}} \chi \beta^3 \cos 3\gamma + \frac{2}{7} \chi^2 \beta^4 \right]. \end{aligned} \tag{8}$$

To extract the mean-field-type deformation, one can minimize the potential function by varying β and γ for the given parameters ε, κ, and χ. The resulting optimal values are denoted by β_{e} and γ_{e}, with which one gets the ground state energy per boson, $E_g = V(\varepsilon, \kappa, \chi, \beta_{\mathrm{e}}, \gamma_{\mathrm{e}})$. Using this procedure, one can not only extract deformations (shapes) of the IBM systems but also identify the associated shape phase transitions [10]. To illustrate the dynamical symmetry limits in the IBM, the corresponding potential surfaces are provided in Fig 1. It is clearly shown from Fig. 1 that the U(5) potential has its minimum at $\beta_{\mathrm{e}} = 0$ indicating the spherical shape, while the SU(3) ones have their minima at either $\gamma_{\mathrm{e}} = 0^{\circ}$ or $\gamma_{\mathrm{e}} = 60^{\circ}$, which correspond to the prolate [SU(3)] and oblate [$\overline{\mathrm{SU(3)}}$], respectively. Clearly, triaxial minimum with $0^{\circ} < \gamma_{\min} < 60^{\circ}$ cannot be generated by these potentials even for the O(6) one with nonzero β as shown in Fig. 1(d), in which the potential, instead, manifests a γ-unstable picture with the potential minimum being independent of the γ variable. In short, the triaxial rotor mode widely used to interpret nuclear excitations [12] cannot be produced from any IBM Hamiltonian up to two-body interactions [13].

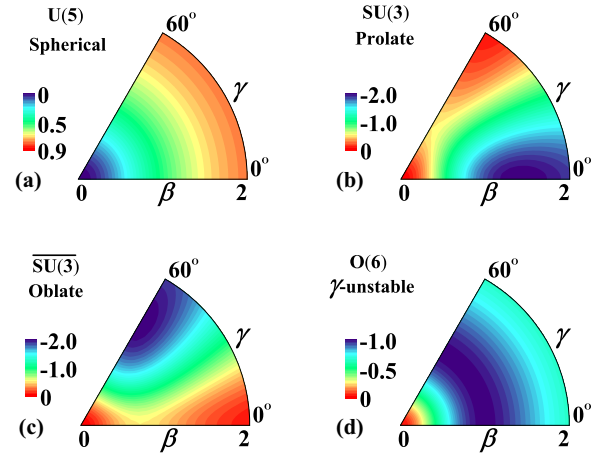

FIG. 1. Potentials surfaces extracted from Eq. (8) with nonzero parameters taken as $\varepsilon = 1.0$ for U(5), $\kappa = -1.0$ and $\chi = 0$ for O(6), and $\kappa = -1.0$ together with $\chi = \mp\sqrt{7}/2$ for SU(3) (prolate and oblate shapes).

In addition to variations in potential surfaces, different modes may present distinct spectral patterns, which can be alternatively identified through specific characteristic quantities. The simplest ones may be the energy ratios, $R_{4/2} \equiv E(4^+_1)/E(2^+_1)$ and $R_{2/2} \equiv E(2^+_2)/E(2^+_1)$, in which $E(2^+_2)$ is the band head energy of the γ or quasi-γ band sensitive to the γ deformation. Typically, $R_{4/2} \approx R_{2/2} \approx 2.0$ for the U(5) mode; $R_{4/2} \approx R_{2/2} \approx 2.5$ for the O(6) mode; and $R_{4/2} \approx 3.3$ but with $R_{2/2} \gg R_{4/2}$ for the SU(3) or $\overline{\mathrm{SU(3)}}$ mode [20]. The trajectories of $R_{4/2}$ vs $R_{2/2}$ calculated from $\hat{H}_{\mathrm{CQ}}$ with $N = 9$ are provided in Fig. 2. In the calculation, the parameters have been expressed as $\varepsilon = (1-\eta)$ and $\kappa = -2\eta$ for convenience, with which the evolution among different modes in the IBM is described by the control parameter $\eta \in [0, 1]$ and $\chi \in [0, -\sqrt{7}/2]$ [21]. Here, we only discuss the cases with $\chi \leqslant 0$ as the Hamiltonian possesses the Z_2 symmetry with $\chi \leftrightarrow -\chi$ [21]. It is shown in Fig. 2 that there is a monotonic change in $R_{2/2}$ as a function of $R_{4/2}$ in between any two modes. Such a monotonic evolution of $R_{2/2}$ against $R_{4/2}$ may be kept for any given χ. Particularly, the narrow region surrounded by the dashed curve is produced from the consistent-Q Hamiltonian. Moreover, it is shown that the area below the consistent-Q region with small $R_{2/2}$ but large $R_{4/2}$ as typically marked by the experimental values of ^{190,192}Os is beyond the scope of the consistent-Q Hamiltonian. Interestingly, this scenario aligns well with the characteristics of triaxial rotor modes, providing strong impetus for the development of the IBM representation of such modes. This endeavor promises to enhance our understanding of the intricate interplay among different collective modes within a unified framework.

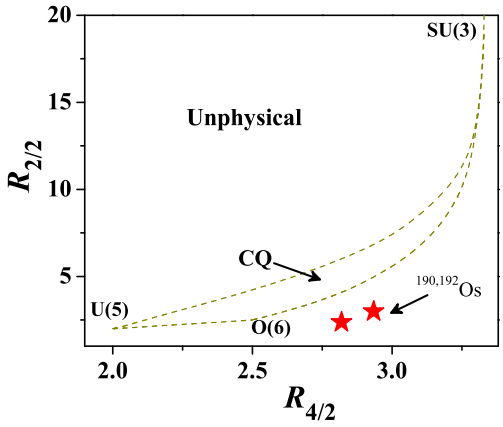

FIG. 2. Trajectories of $R_{2/2}$ vs $R_{4/2}$ obtained from the consistent-Q (CQ) Hamiltonian with $N = 9$. The red stars represent the experimental values of the ratios for ^{190,192}Os [22,23]. No nucleus is observed to exist in the upper left "unphysical" region above the CQ region surrounded by the dashed curve.

III. THE IBM REALIZATION OF TRIAXIAL ROTOR MODES

The algebraic approach established in the shell model description of a quantum rotor [4,5] was employed to construct the triaxial rotor mode in the IBM [6] with the Hamiltonian constructed from the symmetry-conserving operators of the SU(3) ⊃ SO(3) integrity basis [24]. From a group (algebra) theory point of view [3], the su(3) algebraic relation in the large-N limit will contract to the Lie algebra $t_5 \oplus$ so(3) of a quantum rotor. Based on the early works [4–6], an exact mapping between the triaxial rotor and its IBM image was then established in the SU(3) limit of the IBM [7].

The Hamiltonian of a rigid quantum rotor is given by [12,25]

$$\hat{H}_{\rm rot} = A_1\hat{L}_1^2 + A_2\hat{L}_2^2 + A_3\hat{L}_3^2, \tag{9}$$

where L_α is the projection of the angular momentum onto the αth body-fixed principal axis and A_α ($\alpha = 1, 2, 3$) is the corresponding inertia parameter. On the other hand, one can construct three frame-independent scalars [4,5],

$$\hat{L}^2 = \hat{L}_1^2 + \hat{L}_2^2 + \hat{L}_3^2, \tag{10}$$

$$\hat{X}_3^c = \sum_{\alpha\beta}\hat{L}_\alpha\hat{Q}^c_{\alpha\beta}\hat{L}_\beta = \lambda_1\hat{L}_1^2 + \lambda_2\hat{L}_2^2 + \lambda_3\hat{L}_3^2, \tag{11}$$

$$\hat{X}_4^c = \sum_{\alpha\beta\gamma}\hat{L}_\alpha\hat{Q}^c_{\alpha\beta}\hat{Q}^c_{\beta\gamma}\hat{L}_\gamma = \lambda_1^2\hat{L}_1^2 + \lambda_2^2\hat{L}_2^2 + \lambda_3^2\hat{L}_3^2, \tag{12}$$

where the expressions shown on the right-hand side of Eqs. (10)–(12) are obtained in the body-fixed principal axes system. The rotor model operator $\hat{L}_\alpha$ and $\hat{Q}^c_{\alpha\beta}$ are the cartesian form of $\hat{L}_u$ and $\hat{Q}^c_u$ defined as

$$\hat{L}_u = \int \rho(\vec{r})(\vec{r}\times\vec{v})_u\, d\tau, \tag{13}$$

$$\hat{Q}^c_u = \sqrt{16\pi/5}\int \rho(\vec{r})r^2Y_{2u}(\Omega)\, d\tau, \tag{14}$$

where $\rho(\vec{r})$ represents nuclear mass density and the integration is over the whole nuclear volume. With the spherical tensor formulas,

$$\hat{L}_0 = \hat{L}_z, \tag{15}$$

$$\hat{L}_{\pm1} = \mp\frac{1}{\sqrt{2}}(\hat{L}_x \pm i\hat{L}_y), \tag{16}$$

$$\hat{Q}^c_0 = 3\hat{Q}^c_{zz}, \tag{17}$$

$$\hat{Q}^c_{\pm1} = \mp\sqrt{6}\big(\hat{Q}^c_{xz} \pm i\hat{Q}^c_{yz}\big), \tag{18}$$

$$\hat{Q}^c_{\pm2} = \sqrt{\frac{3}{2}}\big(\hat{Q}^c_{xx} - \hat{Q}^c_{yy} \pm 2i\hat{Q}^c_{xy}\big), \tag{19}$$

the scalars given in Eqs. (10)–(12) can be re-expressed as

$$\hat{L}^2 = \sqrt{5}(\hat{L}\times\hat{L})^{(0)}, \tag{20}$$

$$\hat{X}_3^c = \frac{\sqrt{30}}{6}(\hat{L}\times\hat{Q}^c\times\hat{L})^{(0)}, \tag{21}$$

$$\hat{X}_4^c = \frac{5}{18}(\hat{L}\times\hat{Q}^c)^{(1)}\cdot(\hat{L}\times\hat{Q}^c)^{(1)}. \tag{22}$$

Based on Eqs. (10)–(12), one can derive that

$$\hat{L}_\alpha^2 = \big[(\lambda_1\lambda_2\lambda_3)\hat{L}^2 + \lambda_\alpha^2\hat{X}_3^c + \lambda_\alpha\hat{X}_4^c\big]/\big(2\lambda_\alpha^3 + \lambda_1\lambda_2\lambda_3\big), \tag{23}$$

where λ_α with $\alpha = 1, 2, 3$ (or x, y, z) are the expectation values of the quadrupole matrix in the principal-axes system with $\langle\hat{Q}^c_{\alpha\beta}\rangle = \lambda_\alpha\delta_{\alpha\beta}$ satisfying $\lambda_1 + \lambda_2 + \lambda_3 = 0$. Thus, the rotor Hamiltonian (9) can be exactly rewritten as

$$\hat{H}_{\rm rot} = a\hat{L}^2 + b\hat{X}_3^c + c\hat{X}_4^c \tag{24}$$

with

$$\begin{aligned} a &= \sum_\alpha a_\alpha A_\alpha, \quad a_\alpha = \lambda_1\lambda_2\lambda_3/D_\alpha, \\ b &= \sum_\alpha b_\alpha A_\alpha, \quad b_\alpha = \lambda_\alpha^2/D_\alpha, \\ c &= \sum_\alpha c_\alpha A_\alpha, \quad c_\alpha = \lambda_\alpha/D_\alpha, \end{aligned} \tag{25}$$

and

$$D_\alpha = 2\lambda_\alpha^3 + \lambda_1\lambda_2\lambda_3. \tag{26}$$

Since the rotor Hamiltonian (24) is frame independent, an SU(3) algebraic realization of the triaxial rotor can be achieved by replacing $\hat{L}$ and $\hat{Q}^c$ in the Hamiltonian with the SU(3) group generators, $\hat{L}$ and $\hat{Q}$ [4,5]. Accordingly, the values of λ_α can be evaluated from the linear relations suggested in [5] with

$$\begin{aligned} \lambda_1 &= -(\lambda - \mu)/3, \\ \lambda_2 &= -(\lambda + 2\mu + 3)/3, \\ \lambda_3 &= (2\lambda + \mu + 3)/3. \end{aligned} \tag{27}$$

Here, the quantum numbers (λ, μ) are the labels of the irreducible representations (IRREPS) of the SU(3) group, with which the deformation parameter γ can be expressed as [5]

$$\gamma_{\rm S} = \tan^{-1}\left(\frac{\sqrt{3}(\mu+1)}{2\lambda+\mu+3}\right). \tag{28}$$

With the mapping shown above, the rotor image can be established in any nuclear model with the SU(3) symmetry. However, the Hamiltonian (24) does not contain any information of the nuclear ground-state deformation, which will be produced by adding a static (intrinsic) part to the Hamiltonian [6]. As a result, the full IBM Hamiltonian for triaxial rotor can be constructed with two parts [7,8],

$$\hat{H}_{\rm Tri} = \hat{H}_{\rm S} + \hat{H}_{\rm D} \tag{29}$$

with

$$\hat{H}_{\rm S} = \frac{a_1}{N}\hat{C}_2[{\rm SU(3)}] + \frac{a_2}{N^3}\hat{C}_2[{\rm SU(3)}]^2 + \frac{a_3}{N^2}\hat{C}_3[{\rm SU(3)}], \tag{30}$$

$$\hat{H}_{\rm D} = t_1\hat{L}^2 + t_2(\hat{L}\times\hat{Q}\times\hat{L})^{(0)} + t_3(\hat{L}\times\hat{Q})^{(1)}\cdot(\hat{L}\times\hat{Q})^{(1)}, \tag{31}$$

where a_i and t_i $(i = 1, 2, 3)$ are real parameters, $\hat{L}$ and $\hat{Q}$ denote the angular momentum and quadrupole momentum operators defined in the SU(3) basis with

$$\hat{L}_u = \sqrt{10}(d^\dagger\times\tilde{d})^{(1)}_u, \tag{32}$$

$$\hat{Q}_u = 2\sqrt{2}\left[(d^\dagger\times\tilde{s} + s^\dagger\times\tilde{d})^{(2)}_u - \frac{\sqrt{7}}{2}(d^\dagger\times\tilde{d})^{(2)}_u\right]. \tag{33}$$

Clearly, the dynamical part $\hat{H}_{\rm D}$ is just taken from the rotor image $\hat{H}_{\rm rot}$ given in Eq. (24) with the parameters

$$t_1 = a, \quad t_2 = \frac{\sqrt{30}}{6}b, \quad t_3 = \frac{5}{18}c, \tag{34}$$

while the static (intrinsic) part $\hat{H}_{\rm S}$ is employed to determine the ground-state deformation, which involves the SU(3) Casimir operators defined by

$$\hat{C}_2[{\rm SU(3)}] = \tfrac{1}{4}\hat{Q}\cdot\hat{Q} + \tfrac{3}{4}\hat{L}^2, \tag{35}$$

$$\hat{C}_3[{\rm SU(3)}] = -\tfrac{\sqrt{70}}{72}(\hat{Q}\times\hat{Q}\times\hat{Q})^{(0)} - \tfrac{\sqrt{30}}{8}(\hat{L}\times\hat{Q}\times\hat{L})^{(0)}. \tag{36}$$

Eigenvalues of the Casimir operators can be expressed in terms of the SU(3) IRREP with

$$\langle\hat{C}_2[{\rm SU(3)}]\rangle = \lambda^2 + \mu^2 + 3\lambda + 3\mu + \lambda\mu, \tag{37}$$

$$\langle\hat{C}_3[{\rm SU(3)}]\rangle = \tfrac{1}{9}(\lambda-\mu)(2\lambda+\mu+3)(\lambda+2\mu+3)\,. \tag{38}$$

The ground-state energy of the triaxial Hamiltonian (29) is then obtained by $E_g = \langle\hat{H}_{\rm S}\rangle_g = f(\lambda,\mu)$ evaluated at the optimal values (λ_0, μ_0), which is in turn determined by the parameters a_i, as $\hat{H}_{\rm D}$ contributes nothing to the ground-state energy with $L = 0$. Accordingly, the static triaxiality is determined from (λ_0, μ_0) via Eq. (28).

To examine the validity of the designed IBM realization of the rotor model, the results obtained directly from the rotor Hamiltonian (9) with $A_1 : A_2 : A_3 = 3 : 1 : 4$, which corresponds to a very asymmetric situation [25], are provided as examples to compare with those obtained from its IBM image described by Eq. (29). In the IBM calculation, two cases with $N = 36$ and $N = 9$ are considered, respectively. In addition, it is assumed that the asymmetric rotor dynamics is produced from an N-boson system with $\gamma_{\rm S} = 30^\circ$ deformation, which requires $(\lambda_0,\ \mu_0) = (2N/3,\ 2N/3)$ according to Eq. (28). To yield the corresponding ground-state IRREP, the IBM parameters are set by choosing $a_1 : a_2 : a_3 = -\frac{27+10N}{3N} : 1 : 1$. The other parameters are then determined by the mapping scheme described above with $t_1 = 3.0$, $t_2 = 0.0548$, $t_3 = -0.00022$ for $N = 36$ and $t_1 = 3.0$, $t_2 = 0.1956$, $t_3 = -0.00283$ for $N = 9$. The $E2$ operator in the IBM image is simply chosen as the quadrupole operator $\hat{Q}$ defined in Eq. (33), while that in the rotor model is given as

$$T^{E2}_u = \sqrt{\frac{5}{16\pi}}Q_0\left[\cos\gamma\, D_{u,0} + \frac{1}{\sqrt{2}}\sin\gamma\left(D^{(2)}_{u,2} + D^{(2)}_{u,-2}\right)\right], \tag{39}$$

where Q_0 represents the intrinsic charge quadrupole moment. Form Fig. 3, one can find that the spectral pattern generated by the triaxial rotor model can be well reproduced by its the IBM image for both $N = 36$ and $N = 9$. The results confirmed that the rotor modes can indeed be produced in the IBM framework. Meanwhile, one can observe that the $B(E2)$ anomaly characterized by $B_{4/2} < 1.0$ appears in the IBM image at relatively small N as shown in Fig. 3(c), which means that the finite-N effect on the triaxial rotor modes may bring some unconventional feature that is never seen in other collective modes. It will be shown that such a novel feature can be applied to explain the anomalous $E2$ transition phenomena in the neutron-deficient nuclei.

To further understand the IBM image of the rotor model at the mean-filed level, one may work out the potential function corresponding to $\hat{H}_{\rm S}$ using the coherent state method [13], which is given by

$$\begin{aligned} V_{\rm S}(\beta,\gamma) &= \frac{1}{N}\langle\beta,\gamma,N|\hat{H}_{\rm S}|\beta,\gamma,N\rangle|_{N\to\infty} \\ &= a_1\frac{\beta^2}{(1+\beta^2)^2}[8 + 4\sqrt{2}\beta\cos(3\gamma) + \beta^2] \\ &\quad + a_2\frac{\beta^4}{(1+\beta^2)^4}[64 + 32\beta^2 + \beta^4 + 16\beta^2\cos(6\gamma) \\ &\quad + 8\sqrt{2}(8\beta + \beta^3)\cos(3\gamma)] \\ &\quad + a_3\frac{2\beta^3}{9(1+\beta^2)^3}[24\beta + 16\sqrt{2}\cos(3\gamma) \\ &\quad + 6\sqrt{2}\beta^2\cos(3\gamma) + \beta^3\cos(6\gamma)]. \end{aligned} \tag{40}$$

The potential $V_{\rm S}(\beta,\gamma)$ simultaneously describes the classical limit of both $\hat{H}_{\rm S}$ and $\hat{H}_{\rm Tri}$, because the potential for the dynamic part Hamiltonian $\hat{H}_{\rm D}$ disappears in the large-N limit through setting an N-dependent parameter form [8]. With parameters $a_1 : a_2 : a_3 = -\frac{27+10N}{3N} : 1 : 1$ for the IBM image, the obtained classical potential surface with $N \to \infty$ is shown in Fig. 4, which clearly shows that the potential surface is completely different from those presented in Fig. 1. Specifically, it is shown that the potential minimum appears near $\gamma \sim 40^\circ$. This value is close to the one for $\gamma_{\rm S}$ solved from the formula (28), which is more convenient to quantify triaxiality for finite-N systems. Hence, it is clearly shown that

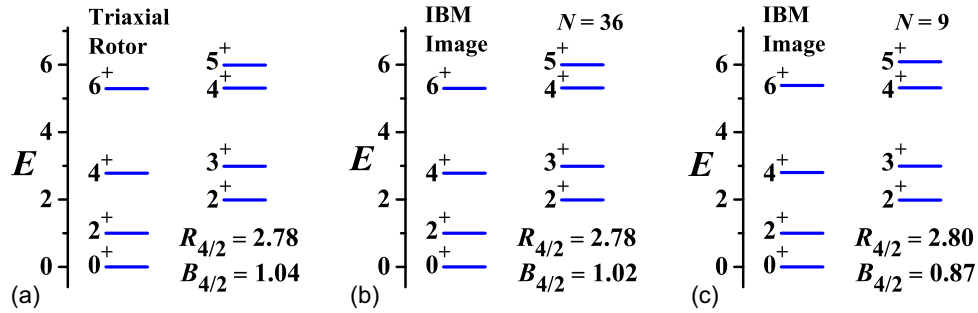

FIG. 3. (a) The level pattern solved from the rotor Hamiltonian (9) with $A_1 : A_2 : A_3 = 3 : 1 : 4$ is shown, where all the levels have been normalized to $E(2_1^+) = 1.0$. (b) The corresponding results solved from the IBM image described by Eq. (29) with the boson number $N = 36$ and other parameters illustrated in the text. (c) The same as in (b) but for $N = 9$. In addition, the typical ratios are defined as $R_{4/2} = \frac{E(4_1^+)}{E(2_1^+)}$ and $B_{4/2} = \frac{B(E2;4_1^+ \to 2_1^+)}{B(E2;2_1^+ \to 0_1^+)}$.

large triaxial deformation can be produced at the mean-field level under the given parameters. In fact, the emergent triaxial deformation can be directly understood from the potential function (40), in which the terms like $\cos(6\gamma)$, which may lead to an asymmetric minimum [13], are involved in contrast to that given in (8). It is thus confirmed that the IBM image of the rotor model indeed yields the novel modes that are different from those described by the consistent-Q Hamiltonian. Therefore, the IBM description can be extended in this way to the triaxial rotor region corresponding to the lower right region of Fig. 2.

IV. DYNAMICAL MIXING OF DIFFERENT MODES

Besides the finite-N corrections, another advantage of the IBM is that the competition or mixing among different collective modes can be easily handled. To analyze the competition between the triaxial rotor and the other modes as well as its indications to the experiments, we adopt the model Hamiltonian with

$$\hat{H} = \epsilon\, \hat{n}_d + \kappa'\, \hat{H}^{\chi}_{\rm Tri}, \tag{41}$$

where ϵ and κ' are two parameters. For the convenience of the subsequent the theoretical discussion, the parameters are reset with $\epsilon = 1 - \eta$ and $\kappa' = -\eta/a_1$, in which η is a control parameter with $\eta \in [0,\ 1]$ and a_1 is the parameter as same as that adopted in Eq. (30). In Eq. (41), $\hat{H}^{\chi}_{\rm Tri}$ is just the rotor mode Hamiltonian $\hat{H}_{\rm Tri}$ defined in Eq. (29) except that the $\hat{Q}$ operator defined in Eq. (33) has been replaced in by

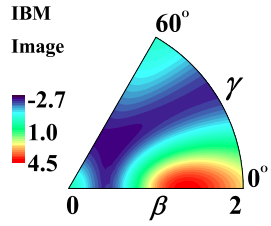

FIG. 4. The potential surface produced from (40) with $a_1 : a_2 : a_3 = -\frac{27+10N}{3N} : 1 : 1$ corresponding to the IBM image shown in Fig. 3 but for $N \to \infty$.

$2\sqrt{2}\hat{Q}^{\chi}$ as defined in Eq. (6). In this way, both the $\hat{L}$ and $\hat{Q}$ operators are still the SU(3) group generators for $\chi = -\sqrt{7}/2$ but become to be the O(6) group generators for $\chi = 0$, which means that the effect of the SU(3) symmetry breaking on the triaxial rotor modes can be examined by varying χ with $\chi \in [-\sqrt{7}/2,\ 0]$. Similarly, the competition between the U(5) mode (spherical vibrator) and triaxial rotor can be described by the Hamiltonian (41) through changing η with $\eta \in [0,\ 1]$ but fixing $\chi = -\sqrt{7}/2$. To provide a parallel comparison, the transitional situations described by the consistent-Q Hamiltonian as a function of η or χ are also considered by resetting the parameters in (4) with $\varepsilon = (1 - \eta)$ and $\kappa = -2\eta$. Then, both the U(5)-SU(3) and the U(5)-O(6) transitional cases can be realized through varying η with $\eta \in [0,\ 1]$ but fixing $\chi = -\sqrt{7}/2$ and $\chi = 0$, respectively, while the SU(3)-O(6) transition is described by fixing $\eta = 1$ but varying χ with $\chi \in [-\sqrt{7}/2, 0]$. Note that the factor $\frac{1}{a_1}$ added in Eq. (41) is just used to be consistent with the parametrization in the consistent-Q formalism (4).

In the following, we focus on the typical ratios, $R_{4/2}$, $R_{2/2}$, and $B_{4/2}$ defined previously, since these ratios can be used not only to characterize the evolution between different modes, but also to signify the occurrence of the $B(E2)$ anomaly. The calculated results as a function of η or χ are shown in Fig. 5. In the calculation for the rotor image described by $\hat{H}^{\chi}_{\rm Tri}$, we select two sets of parameters: one is taken as the same as that adopted for Fig. 3(c), namely, $a_1 : a_2 : a_3 = -\frac{27+10N}{3N} : 1 : 1$, which will generate the ground-state SU(3) IRREP $(\lambda_0, \mu_0) = (6, 6)$ corresponding to $\gamma_S = 30^\circ$; another one is set by choosing $a_1 : a_2 : a_3 = -\frac{27+10N}{3N} : 1 : 0.9$, which yields $(\lambda_0, \mu_0) = (10, 4)$ corresponding to $\gamma_S = 17.8^\circ$. In contrast to the former case yielding $B_{4/2} < 1.0$, the latter case generates $B_{4/2} > 1.0$, which means no $B(E2)$ anomaly occurring in the latter case.

As seen from Fig. 5(a), the ratio $R_{4/2}$ increases with increasing of η in all the cases except for a small fluctuation appearing near one of the rotor images. Nonetheless, the ratio is always kept within a normal range with $2.0 \leqslant R_{4/2} \leqslant 3.33$. However, the ratio $B_{4/2}$ in the transitional case involving the rotor mode (denoted by Image) corresponding to $\gamma_S = 30^\circ$ reaches an unexpectedly low value with $B_{4/2} \sim 0.5$ as shown

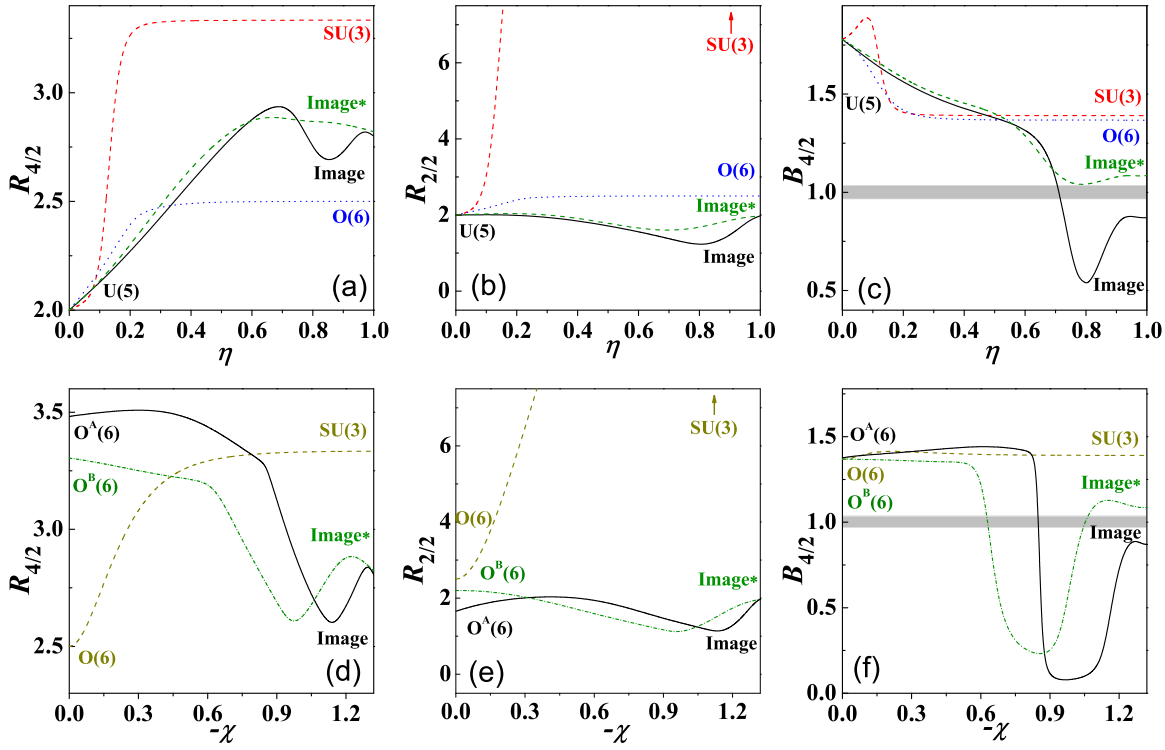

FIG. 5. Upper: The $R_{4/2}$ (a), $R_{2/2}$ (b), and $B_{4/2}$ (c) values solved from Eq. (41) as a function of η after fixing $\chi = -\sqrt{7}/2$ are shown to compare with those for the U(5)-SU(3) and U(5)-O(6) transitions described by the consistent-Q Hamiltonian. Lower: The $R_{4/2}$ (d), $R_{2/2}$ (e), and $B_{4/2}$ (f) values solved from Eq. (41) as a function of χ after fixing $\eta = 1$ are shown to compare with the results for the O(6)-SU(3) transition described by the consistent-Q Hamiltonian. The curves denoted by Image and Image* represent the results solved from the rotor image with $\gamma_S = 30^\circ$ ($a_1 : a_2 : a_3 = -\frac{27+10N}{3N} : 1 : 1$) and $\gamma_S = 17.8^\circ$ ($-\frac{27+10N}{3N} : 1 : 0.9$), respectively. The total boson number adopted in the calculations is $N = 9$. O(6) in each case indicates that the values are obtained for $\chi = 0$ and the grey color in (c) and (f) is used to symbolize $B_{4/2} = 1.0$.

in Fig. 5(c). It means that the competition from the U(5) mode will enhance the $B(E2)$ anomaly feature emerging from the triaxial rotor mode. In contrast, another case involving the rotor mode with less triaxial deformation ($\gamma_S = 17.8^\circ$) still keeps $B_{4/2} > 1.0$ within $\eta \in [0,\ 1]$. Meanwhile, the ratio $R_{2/2}$ in different cases maintains to be small as shown in Fig. 5(b) except in the U(5)-SU(3) transition case, in which the ratio $R_{2/2}$ increases drastically with increasing of η as expected.

An even more striking feature shown in Figs. 5(d)–5(f) is that the $B_{4/2}$ ratio may drop to very low value for a wide range of χ during the O(6)-SU(3) transition, while $R_{4/2} \geqslant 2.5$ is kept. The results indicate that the symmetry breaking can drive a less γ-deformed system (such as that denoted by Image*) from $B_{4/2} > 1.0$ to $B_{4/2} < 1.0$, while the ratio $R_{2/2}$ maintains to be small except in the axial SU(3) symmetry case. In short, small $B_{4/2}$ ratio is relatively easier to be produced in a soft triaxial system, which thus provides a new clue to explain the $B(E2)$ anomaly phenomena observed in experiment. Here, a soft triaxial system means that deviating from the SU(3) symmetry because the exact SU(3) realization of a triaxial rotor may yield specific γ_S value via Eq. (28) corresponding to γ rigid deformation.

V. APPLICATIONS TO Os NUCLEI

As a preliminary application of the triaxial rotor description, two neutron-rich isotopes ^{190,192}Os are chosen to be considered and compared with the two neutron-deficient counterparts ^{168,170}Os, which possesses the same number of bosons (the number of valence nucleon pairs) as the former two nuclei with $N = 8,\ 9$. The former two Os nuclei with large $R_{4/2}$ but small $R_{2/2}$ as indicated in Fig. 2 were suggested to be the good candidates for triaxial nuclei [26], while the latter two Os nuclei were observed with $R_{4/2} > 2.5$ but $B_{4/2} < 1.0$ [27,28]. Undoubtedly, the spectral features in these Os nuclei can not be explained from the traditional modes in the IBM [10], which thus provides a chance to test the present theoretical scheme. The model Hamiltonian is given by Eq. (41). In experiments, the available data for the neutron-rich Os nuclei are relatively more abundant as shown in Fig. 6 and Table I, where the level patterns and some $B(E2)$ values in ^{190,192}Os are provided in comparison with the corresponding theoretical results. In the model calculation, it is assumed that triaxial deformation is built from the maximally triaxial IRREP of SU(3), which are $(\lambda_0, \mu_0) = (6, 6)$ for $N = 9$ and $(\lambda_0, \mu_0) = (4, 6)$ for $N = 8$. Accordingly, $\gamma_S = 30^\circ$ and $\gamma_S = 35^\circ$ are yielded from the two ground-state IRREPs, which can be generated by $\hat{H}^{\chi}_{\rm Tri}$ through setting the parameters $a_1 : a_2 : a_3 = -4.0 : 1.0 : 1.0$ and $-4.46 : 1.0 : 1.0$, respectively.

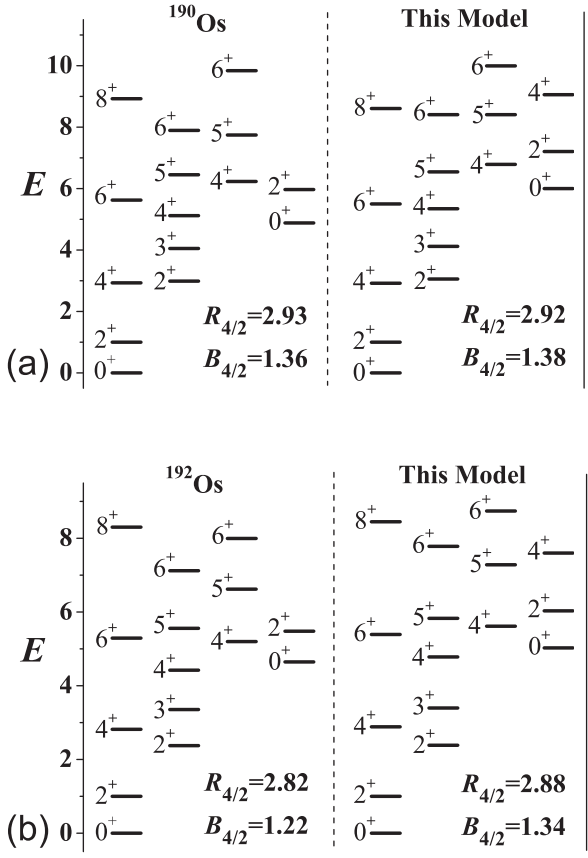

FIG. 6. The level patterns of ^{190,192}Os [22,23] with all the levels normalized to $E(2_1) = 1.0$ are shown to compare with those obtained from the model Hamiltonian (41) with the parameters as illustrated in the text.

TABLE I. The model fits for the $B(E2)$ transitions (unit in W.u.) in ^{190}Os and ^{192}Os with the effective charges (in $\sqrt{\text{W.u.}}$) adopted as $e = 2.479$ and $e = 2.464$, respectively.

Transition	^{190}Os	This model	Transition	^{192}Os	This model
$2_1^+ \to 0_1^+$	71.9(21)	71.90	$2_1^+ \to 0_1^+$	62.1(7)	62.10
$4_1^+ \to 2_1^+$	105(6)	98.90	$4_1^+ \to 2_1^+$	75.6(20)	83.15
$6_1^+ \to 4_1^+$	113(10)	105.36	$6_1^+ \to 4_1^+$	$100(^{+5}_{-3})$	89.86
$6_1^+ \to 4_2^+$	6(4)	6.80	$6_1^+ \to 4_2^+$	–	4.51
$8_1^+ \to 6_1^+$	137(20)	99.93	$8_1^+ \to 6_1^+$	115(6)	82.07
$0_2^+ \to 2_1^+$	2.2(5)	0.12	$0_2^+ \to 2_1^+$	0.57(12)	0.30
$0_2^+ \to 2_2^+$	23(7)	57.54	$0_2^+ \to 2_2^+$	$30.4(^{+30}_{-23})$	45.02
$2_2^+ \to 0_1^+$	5.9(6)	7.76	$2_2^+ \to 0_1^+$	$5.62(^{+21}_{-12})$	5.33
$2_2^+ \to 2_1^+$	33(4)	51.00	$2_2^+ \to 2_1^+$	$46(^{+26}_{-12})$	58.30
$4_2^+ \to 2_1^+$	0.68(6)	0.12	$4_2^+ \to 2_1^+$	0.29(3)	0.08
$4_2^+ \to 4_1^+$	30(4)	38.25	$4_2^+ \to 4_1^+$	$30.9(^{+36}_{-18})$	32.48
$4_2^+ \to 2_2^+$	53(5)	45.14	$4_2^+ \to 2_2^+$	$45.2(^{+14}_{-18})$	39.17
$4_2^+ \to 3_1^+$	65(13)	38.15	$4_2^+ \to 3_1^+$	–	11.03
$6_2^+ \to 4_1^+$	<0.8	0.04	$6_2^+ \to 4_1^+$	–	0.077
$6_2^+ \to 4_2^+$	65(13)	59.59	$6_2^+ \to 4_2^+$	$52(^{+3}_{-6})$	42.60
$6_2^+ \to 6_1^+$	31(8)	24.23	$6_2^+ \to 6_1^+$	$26(^{+55}_{-21})$	17.78
$4_3^+ \to 2_1^+$	0.001(4)	0.02	$4_3^+ \to 2_1^+$	$0.22(^{+21}_{-10})$	0.17
$4_3^+ \to 4_1^+$	0.084(17)	0.001	$4_3^+ \to 4_1^+$	–	0.081
$4_3^+ \to 2_2^+$	7.6(15)	10.77	$4_3^+ \to 2_2^+$	$10.6(^{+18}_{-21})$	3.57
$4_3^+ \to 3_1^+$	27(6)	38.73	$4_3^+ \to 3_1^+$	$56(^{+14}_{-15})$	42.02
$4_3^+ \to 4_2^+$	14(6)	49.61	$4_3^+ \to 4_2^+$	$24(^{+6}_{-7})$	78.75
$2_3^+ \to 2_2^+$	–	3.91	$2_3^+ \to 2_2^+$	0.41(4)	3.41
$2_3^+ \to 3_1^+$	–	31.25	$2_3^+ \to 3_1^+$	1.1(10)	20.71

In fact, the γ values extracted from the present model are in good qualitative agreement with those obtained from the proxy-SU(3) scheme [29] using the shell model IRREPs for the highest weight states as given in [30], where the results indicate $\gamma = 30^\circ$ for ^{190}Os and $\gamma = 40.4^\circ$ for ^{192}Os, respectively. Here, we have fixed $\chi = -1.32$ in the calculation for the two neutron-rich Os nuclei. The other parameters in $\hat{H}^{\chi}_{\text{Tri}}$ for ^{190}Os (^{192}Os) can be evaluated via Eqs. (25)–(27) with the inertial parameters set by $A_1 : A_2 : A_3 = 51 : 17 : 136$ (18 : 16 : 96), which are roughly estimated from the low-lying energies in experiments. Based on the mapping scheme, $t_1 : t_2 : t_3 = 0.0357 : 0.0054 : 0.0001$ (0.0432 : 0.0063 : 0.0001) for ^{190}Os (^{192}Os) is obtained. After fixing the triaxial rotor mode based on the mapping scheme, the two parameters (in keV) in the model Hamiltonian are determined in fitting to the experimental data with $\varepsilon = 327.1$ (291.1) and $\kappa' = 218.1$ (264.6) for ^{190}Os (^{192}Os).

Similarly, the model parameters for ^{168,170}Os can be determined from the mapping scheme in the same way. Due to the same boson numbers given to them, the maximal triaxial IRREPs for the two neutron-deficient nuclei are also obtained as $(\lambda_0, \mu_0) = (6, 6)$ for $N = 9$ and $(\lambda_0, \mu_0) = (4, 6)$ for $N = 8$, which means that the obtained γ values would be as same as those for ^{190,192}Os. However, the γ deformations in the two neutron-deficient Os nuclei are supposed to be much softer [27,28] than in the neutron-rich ones. This point in the present model will be additionally reflected from the parameter $|\chi| < 1.32$ [see Fig. 5(f)]. Specifically, the parameters for ^{168}Os (^{170}Os) are adopted by $\varepsilon = 66.1$ (93.2) keV, $\kappa' = 82.6$ (66.6) keV together with $a_1 : a_2 : a_3 = -4.46 : 1.0 : 1.0$ ($-4.0 : 1.0 : 1.0$) and $t_1 : t_2 : t_3 = 0.5159 : 0.0606 : -0.0001$ ($0.5400 : 0.0493 : -0.0003$). In addition, $\chi = -0.8$ and $\chi = -1.0$ are taken for ^{168}Os and ^{170}Os, respectively, corresponding to softer triaxial rotor images. By contrast, ^{168}Os (^{170}Os) with ten (12) valence neutron particles in the proxy-SU(3) scheme has the shell model IRREP for the highest weight state being very different from that for its neutron-rich partner ^{192}Os (^{190}Os) with ten (12) valence neutron holes, thus giving the relatively smaller triaxial deformations with $\gamma \simeq 20^\circ$ ($\gamma \simeq 14^\circ$). In comparison with the neutron-rich Os nuclei, the low-lying data for the neutron-deficient Os nuclei are scarce, and only those for the yrast states in ^{168,170}Os are provided in comparison with the model results.

It is shown in Fig. 6 that the level patterns of ^{190}Os and ^{192}Os are well reproduced by the model. Especially, the lowest excitation energy in the two nuclei with $E(2_1) = 186.7$keV and 205.8keV, respectively, is well reproduced. As further

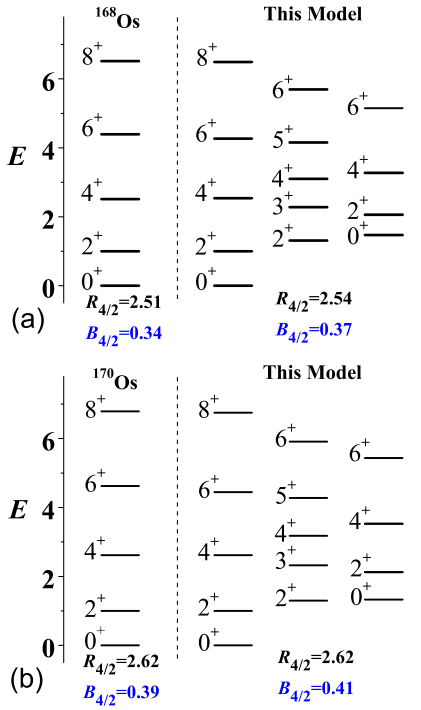

FIG. 7. The level patterns of ^{168,170}Os [27,28] will all the levels normalized to $E(2_1) = 1.0$ are shown to those solved from the model Hamiltonian (41) with the parameters as mentioned in the text.

shown in Table I, the consistency between experimental and theoretical results is evident, particularly in the calculated $B(E2)$ values, notably for strong intraband transitions and weak interband transitions. The only discrepancy arises from the overestimated $B(E2; 2_3^+ \to 3_1^+)$ for ^{192}Os, which could potentially be rectified by incorporating other modes into the model Hamiltonian. The low-lying properties of the neutron-rich Os nuclei seem to find reasonable explanation through the mixing of triaxial rotor mode with the vibrational U(5) mode, expanding the IBM descriptions beyond the traditional modes, as depicted in Fig. 2. For the neutron-deficient nuclei, ^{168}Os and ^{170}Os, the theoretical results successfully reproduce the yrast levels and the $B(E2)$ anomaly characterized by $B_{4/2} < 1.0$, as illustrated in Fig. 7. Additionally, theoretical calculations predict very low β and γ bands for these nuclei, mirroring the neutron-rich cases as depicted in Fig. 6. It is noteworthy from Table II that the

TABLE II. The calculated $B(E2)$ values normalized to $B(E2; 2_1^+ \to 0_1^+) = 1.0$ are shown to compare with those available for ^{168}Os [27] and ^{170}Os [28].

Transition	^{168}Os	This model	Transition	^{170}Os	This model
$2_1^+ \to 0_1^+$	1.0	1.0	$2_1^+ \to 0_1^+$	1.0	1.0
$4_1^+ \to 2_1^+$	**0.34(18)**	**0.372**	$4_1^+ \to 2_1^+$	**0.38(11)**	**0.409**
$6_1^+ \to 4_1^+$	–	0.694	$6_1^+ \to 4_1^+$	–	0.709
$2_2^+ \to 0_1^+$	–	0.007	$2_2^+ \to 0_1^+$	–	0.008
$0_2^+ \to 2_1^+$	–	0.0001	$0_2^+ \to 2_1^+$	–	0.067

$B(E2)$ anomaly, $B(E2; L_1^+ \to (L-2)_1^+)/B(E2; 2_1^+ \to 0_1^+) < 1.0$, persists to the yrast states of higher spins. While a more quantitative prediction requires further experimental constraints, the current analysis strongly suggests the possibility of a soft triaxial deformation in these neutron-deficient nuclei exhibiting the $B(E2)$ anomaly, given that the model parameters are fully constrained by the mapping from the triaxial rotor. This finding is consistent with the mean-field calculations [28,31]. Moreover, collective modes with $B_{4/2} < 1.0$ are observed not only in intermediate-mass nuclei [32], but also in light nuclei [33]. For instance, no-core symplectic shell model (NCSpM) calculations [33] suggest that small SU(3) irreducible representations, such as $(\lambda, \mu) = (4, 2)$ and $(6, 2)$, may significantly contribute to the low-lying yrast states of ^{20}Mg and ^{20}O. Based on this analysis, it can be inferred that small triaxial (λ, μ) may induce triaxial deformation associated with $B_{4/2} < 1.0$. This conclusion is supported not only by the NCSpM description [33] but also by the possible triaxiality in ^{20}Mg analyzed in [34].

It is worth noting that the $B_{4/2} < 1.0$ phenomenon was recently explained in [35] from the prohibition of $E2$ transitions between different SU(3) irreducible representations using an IBM Hamiltonian similar to the extended consistent-Q formula [17], which actually allows for soft triaxial deformations in a narrow parameter region. Further extensions of the study in [35] were recently made to analyze nuclear spectra related to the prolate-oblate shape transition [36] and the associated emergent O(5)-like γ-soft modes [37–39], showing the rich SU(3) dynamics in the IBM after involving the high-order terms. In these studies, the second- and third-order SU(3) symmetry-conserving terms as defined in Eqs. (35)–(36) are particularly addressed. Since the leading SU(3) IRREPs generated by $\hat{C}_2[\mathrm{SU}(3)]$ and $\hat{C}_3[\mathrm{SU}(3)]$ are $(\lambda, \mu) = (2N, 0)$ and $(0, N)$, respectively, it is not surprising that these SU(3) terms may play the central role in demonstrating the spectral evolution in the prolate-oblate shape transition [40]. In contrast, the high-order SU(3) symmetry terms in the present scheme are introduced in a compact way via the SU(3) mapping of a quantum rotor. In particular, it is shown that the fourth-order term is necessary to generate an algebraic image of the triaxial rotor, which can not only be applied to yield a soft triaxial rotor mode associated with $B_{4/2} < 1.0$ as revealed in the recent study [8] and even earlier work [7] [see Fig. 2(b)], but also generate a relatively rigid rotor mode like that occurring for ^{190,192}Os as discussed above. Another point worth mentioning is the asymmetry between prolate and oblate in the SU(3) IBM scheme [36,40], which is mainly caused by the difference between the eigenvalues of $\hat{C}_2[\mathrm{SU}(3)]$ (prolate) and $\hat{C}_3[\mathrm{SU}(3)]$ (oblate). The resulting asymmetric structural evolutions agree well with the realistic situations like the prolate-oblate shape transitions occurring in the $A = 190$ mass region [36,40]. Nonetheless, the IBM cannot tell which nucleus is prolate, oblate or triaxial solely based on the boson number N. An answer to such a kind of asymmetry between prolate and oblate undoubtedly needs a microscopic model such as the proxy-SU(3) shell model scheme [29], by which one can predict not only the locus of the prolate-oblate shape transition but also the dominance of prolate shapes in experiments [30].

It is thus highly expected to find a suitable way to extend the current IBM-based analysis into the proxy-SU(3) scheme.

VI. SUMMARY

In summary, we propose a scheme for describing triaxial dynamics in finite-N systems by constructing the IBM image of the rotor model Hamiltonian using the SU(3) mapping procedure. The resulting model dynamics are meticulously analyzed, revealing novel features not anticipated in traditional collective modes. Particularly noteworthy is the emergence of the $B(E2)$ anomaly feature, characterized by $R_{4/2} > 2$ and $B_{4/2} < 1$, which naturally arises from the IBM image of the triaxial rotor and is significantly enhanced in soft triaxial cases such as in the U(5)-SU(3) and O(6)-SU(3) transitions, as observed in Fig. 5. As applications, the model Hamiltonian involving triaxial rotor modes is employed to describe four Os nuclei, all presumed to be triaxially deformed. The results demonstrate that the triaxial model not only excellently reproduces the low-lying structures of the two neutron-rich Os isotopes (^{190,192}Os with relatively rigid triaxial deformation) but also provides a satisfactory description of the yrast levels and the suppressed $B_{4/2}$ ratios in the two neutron-deficient Os isotopes (^{168,170}Os with soft triaxial deformation) [27,28]. This characteristic is noteworthy and merits further examination in microscopic models such as the large-scale shell and beyond mean field/generator coordinate method, which have yet to explain the anomalous $B_{4/2}$ feature.

It is notable that all typical nuclear modes, including the triaxial rotor, can be treated on equal footing within the proposed algebraic scheme. Additionally, similar $B(E2)$ anomalies in yrast states have been observed in adjacent odd Os nuclei, ^{169,171}Os [41]. For future research, it would be intriguing to explore the influence of odd neutrons by extending our formalism to odd-A systems.

ACKNOWLEDGMENTS

Support from the National Natural Science Foundation of China under Grants No. 12375113, No. 11875158, and No. 12175097 and from LSU through its Sponsored Research Rebate Program as well as the LSU Foundation's Distinguished Research Professorship Program is acknowledged.

[1] A. Bohr and B. R. Mottelson, *Nuclear Structure II* (Benjamin, New York, 1975).
[2] J. P. Elliott, Proc. R. Soc. Lond. A **245**, 128 (1958); **245**, 562 (1958); J. P. Elliott and M. Harvey, *ibid.* **272**, 557 (1963); J. P. Elliott and C. E. Wilsdon, *ibid.* **302**, 509 (1968).
[3] H. Ui, Prog. Theor. Phys. **44**, 153 (1970).
[4] Y. Leschber and J. P. Draayer, Phys. Lett. B **190**, 1 (1987).
[5] O. Castaños, J. P. Draayer, and Y. Leschber, Z. Phys. A **329**, 33 (1988).
[6] Y. F. Smirnov, N. A. Smirnova, and P. Van Isacker, Phys. Rev. C **61**, 041302(R) (2000).
[7] Y. Zhang, F. Pan, L. R. Dai, and J. P. Draayer, Phys. Rev. C **90**, 044310 (2014).
[8] Y. Zhang, Y. W. He, D. Karlsson, C. Qi, F. Pan, and J. P. Draayer, Phys. Lett. B **834**, 137443 (2022).
[9] V. K. B. Kota, *SU(3) Symmetry in Atomic Nuclei* (Springer, Singapore, 2020).
[10] F. Iachello and A. Arima, *The Interacting Boson Model* (Cambridge University, Cambridge, 1987).
[11] D. D. Warner and R. F. Casten, Phys. Rev. C **28**, 1798 (1983).
[12] A. S. Davydov and G. F. Filippov, Nucl. Phys. **8**, 237 (1958).
[13] P. Van Isacker and J. Q. Chen, Phys. Rev. C **24**, 684 (1981).
[14] K. Heyde, P. Van Isacker, M. Waroquier, and J. Moreau, Phys. Rev. C **29**, 1420 (1984).
[15] J. E. García-Ramos, C. E. Alonso, J. M. Arias, and P. Van Isacker, Phys. Rev. C **61**, 047305 (2000).
[16] J. E. García-Ramos, J. M. Arias, and P. Van Isacker, Phys. Rev. C **62**, 064309 (2000).
[17] L. Fortunato, C. E. Alonso, J. M. Arias, J. E. García-Ramos, and A. Vitturi, Phys. Rev. C **84**, 014326 (2011).
[18] W. Teng, S. N. Wang, Y. Zhang, and L. Fortunato, Phys. Scr. **99**, 015305 (2024).
[19] L. Wilets and M. Jean, Phys. Rev. **102**, 788 (1956).
[20] J. Jolie, R. F. Casten, P. von Brentano, and V. Werner, Phys. Rev. Lett. **87**, 162501 (2001).
[21] F. Iachello and N. V. Zamfir, Phys. Rev. Lett. **92**, 212501 (2004).
[22] B. Singh, Nucl. Data Sheets **99**, 275 (2003).
[23] C. M. Baglin, Nucl. Data Sheets **113**, 1871 (2012).
[24] G. Vanden Berghe, H. E. De Meyer, and P. Van Isacker, Phys. Rev. C **32**, 1049 (1985).
[25] J. L. Wood, A.-M. Oros-Peusquens, R. Zaballa, J. M. Allmond, and W. D. Kulp, Phys. Rev. C **70**, 024308 (2004).
[26] J. M. Allmond, R. Zaballa, A.-M. Oros-Peusquens, W. D. Kulp, and J. L. Wood, Phys. Rev. C **78**, 014302 (2008).
[27] T. Grahn, S. Stolze, D. T. Joss, R. D. Page, B. Saygı, D. O'Donnell *et al.*, Phys. Rev. C **94**, 044327 (2016).
[28] A. Goasduff *et al.*, Phys. Rev. C **100**, 034302 (2019).
[29] D. Bonatsos, I. E. Assimakis, N. Minkov, Andriana Martinou, R. B. Cakirli, R. F. Casten, and K. Blaum, Phys. Rev. C **95**, 064325 (2017).
[30] D. Bonatsos, I. E. Assimakis, N. Minkov, Andriana Martinou, S. Sarantopoulou, R. B. Cakirli, R. F. Casten, and K. Blaum, Phys. Rev. C **95**, 064326 (2017).
[31] R. Rodríguez-Guzmán, P. Sarriguren, L. M. Robledo, and J. E. García-Ramos, Phys. Rev. C **81**, 024310 (2010).
[32] D. Hertz-Kintish, L. Zamick, and S. J. Q. Robinson, Phys. Rev. C **90**, 034307 (2014).
[33] G. K. Tobin, M. C. Ferriss, K. D. Launey, T. Dytrych, J. P. Draayer, A. C. Dreyfuss, and C. Bahri, Phys. Rev. C **89**, 034312 (2014).
[34] P. Mitra, G. Gangopadhyay, and B. Malakar, Phys. Rev. C **65**, 034329 (2002).
[35] T. Wang, Europhys. Lett. **129**, 52001 (2020).
[36] T. Wang, B. C. He, D. K. Li, and C. X. Zhou, Phys. Rev. C **107**, 064322 (2023).
[37] T. Wang, Chin. Phys. C **46**, 074101 (2022).
[38] T. Wang, B. C. He, C. X. Zhou, D. K. Li, and L. Fortunato, arXiv:2308.11231.
[39] T. Wang, X. Chen, and Y. Zhang, arXiv:2404.08198.
[40] Y. Zhang, F. Pan, Y. X. Liu, Y. A. Luo, and J. P. Draayer, Phys. Rev. C **85**, 064312 (2012).
[41] W. Zhang *et al.*, Phys. Lett. B **820**, 136527 (2021).